DOI: 10.1002/ ((please add manuscript number))
Article type: Full paper

Controlling Nucleation and Growth of Metal Halide Perovskite Thin-films for High Efficiency Perovskite Solar Cells

Nobuya Sakai, Zhiping Wang, Victor M. Burlakov, Jongchul Lim, David McMeekin, Sandeep Pathak and Henry J. Snaith[*]

[*] Henry J. Snaith
Department of Physics
University of Oxford
Clarendon Laboratory
Parks Road
Oxford OX1 3PU
United Kingdom
E-mail: Henry.Snaith@physics.ox.ac.uk

Keywords: Perovskite photovoltaic; Thin-film crystallization; Nucleation; lead halide mix

Abstract

Metal halide perovskite thin-films can be crystallized via a broad range of solution based routes. However, the quality of the final films is strongly dependent upon small changes in solution composition and processing parameters. Here, we demonstrate that a fractional substitution of $PbCl_2$ with PbI_2 in the $3CH_3NH_3I$:$PbCl_2$ mixed-halide starting solution has a profound influence upon the ensuing thin film crystallization. The presence of PbI_2 in the precursor induces a uniform distribution of regular quadrilateral shaped $CH_3NH_3PbI_3$ perovskite crystals in as-cast films, which subsequently grow to form pinhole-free perovskite films with highly-crystalline domains. With this new formulation of $3CH_3NH_3I$:$0.98PbCl_2$:$0.02PbI_2$ we achieve a 19.1% current-voltage measured power conversion efficiency and a 17.2% stabilized power output in regular planar heterojunction solar cells.

1. Introduction

One of the primary factors which excites the scientific community about perovskites, is rooted in the ability to solution process the metal halide perovskites and crystallizes the thin films at low temperature. This promises to deliver low fabrication cost in manufacturing, and will enable solar cells to be fabricated on a range of substrates, including light weight flexible electrodes.[1,2] The record power conversion efficiency of organic-inorganic lead halide perovskite ($HC(NH_2)_2PbX_3$ or $CH_3NH_3PbX_3$) solar cells has increased significantly beyond 20%.[3–5] Some of the highest efficiency solar cells are fabricated from an “anti-solvent” quenching, or solvent exchange method, whereby the perovskite film is drenched with an anti-solvent while it is being spin-coated on the substrate.[4] This leads to accelerated crystallization and smooth films.[6–8] However, this adds a complication to potential manufacturing, and there is yet to be a proposed route to extend this method from spin-coating to larger area solution coating methods, such as slot-die coating[9,10], ink-jet printing[11] or doctor-blade coating[12].

For the single step solution processing routes which employ an excess of the organic component (i.e. 3 methyl ammonium (MA)I:$PbCl_2$), during the crystallization process the nucleation crystals are embedded in matrix of an intermediate “precursor phase”, and with subsequent annealing these nuclei crystals grow in size, assimilating the precursor phase.[13–15] Through this route, very large crystalline grains can be formed, which should be beneficial for reducing recombination losses at the grain boundaries.[16,17] However, if the available precursor phase (within which the grains are growing) is consumed by the growing perovskite domains before the domains impinge upon each other, then voids will be left between the grains in the form of pinholes. Hence, the rate of crystallization plays a critical role in determining the grain size, shape, surface coverage and crystal strain.[8,18,19]

Recently, Nazeerudin and coworkers reported the adding “excess” PbI_2 into the previously stoichiometric MAI:PbI_2 starting solution formulation, resulted in higher efficiency than the conventional stoichiometric composition.[19] They observed larger crystals in the films processed from the solutions containing excess PbI_2, and suggested that the formation of larger crystals is intrinsically related to a more relaxed lattice structure formed during the crystallization process. They infer that the subsequently improved solar cell performance is derived from residual PbI_2 in the film, considered to function as a grain surface passivation layer.[20] It would therefore be useful to better understand the interplay between starting solution and final perovskite films quality. With the intention to achieve both large grains of high crystalline quality, and uniform films with no pinholes, it appears sensible to revisit the formulation of the excess-organic mixed halide deposition route, specifically understanding the interplay of varying the metal-halide source upon nucleation and growth and final film quality. Here, we have discovered that by substituting only 2 mol% of $PbCl_2$ with the PbI_2 in the mix-halide precursor composition (3MAI:$PbCl_2$) we transform the nucleation and growth process in thin film fabrication. The presence of the PbI_2 results in uniformly distributed quadrilateral shaped crystallites of tens of microns in size, just after the casting of the precursor film, as

opposed to “precursor crystals” which usually proceed crystallization with this mixed-halide recipe.[13] These crystals grow and impinge to form pinhole free films with highly-crystalline domains. By incorporating these films into regular planar heterojunction perovskite solar cells fabricated in humidity controlled air, we achieved 19.1% current-density voltage (JV) measured power conversion efficiency and 17.2% stabilized power output (SPO), while attaining a higher degree of reproducibility.

2. Results and discussion

We fabricate a range of perovskite thin films from dimethylformamide (DMF) solutions containing different PbI_2 concentrations. We keep the ratio of methylammonium (MA) to Pb at 3:1, but incrementally substitute $PbCl_2$ with PbI_2 such that the starting solution contains $3MAI:(1-x)PbCl_2:xPbI_2$, where x = 0, 0.02, 0.05, 0.4 and 1. Throughout the manuscript we will refer to the perovskite films fabricated from solutions containing differing compositions as the “x = 0” (or x = 0.02, 0.05, 0.4 and 1) film or sample. For the fabrication process, we spin-coat the solutions at room temperature in a humidity controlled (relative humidity ~30%) air dry box, and “blow dry” the films prior to annealing. The blow drying process accelerates the solvent drying and results in much improved surface coverage of the film[21] (we give full experimental details in the method section). We observed a clear difference in the morphology of the films fabricated from the different solution compositions, which we visualize in the scanning electron microscopy (SEM) images in **Figure 1**. For the perovskite films fabricated from the mixed halide precursor; where x = 0 ($3MAI:PbCl_2$), we observe large perovskite grains ranging from 0.5 to 1 μm in size, accompanied by a few pinholes. Interestingly, incorporating 2 mol% of PbI_2, i.e. x = 0.02 ($3MAI:0.98PbCl_2:0.02PbI_2$) in the mixed halide precursor, the fully crystallized films show a rectangular shape crystalline domains. Furthermore, we observe very few pinholes in the perovskite film showing almost 100% surface coverage (**Figure 1b** and **1b’**). However, for films processed from precursors with x = 0.05, 0.4 and 1, the films lose

the ordered rectangular-crystal morphology. Additionally, we find that the higher PbI_2 content negatively affect to the film morphology, which exhibit poor surface coverage with the appearance of pin-holes and cracks.

In order to probe whether or how the crystallinity has been influenced by the variations in the starting perovskite solutions, we perform X-ray diffraction (XRD) on the fully crystallized perovskite films, which we show in **Figure 2 a.** We observe similar peak positions for the perovskite films from all the precursors, which confirms their tetragonal crystal structure (*I4/mcm*) with two distinct (110) and (220) diffraction peaks at 14.2° and 28.5°, respectively.[22] As we show in Figure S1, both of the (110) and (220) peaks show almost doubled peak intensity in the film with x = 0.02 with respect to the x = 0 analogue, indicating a higher degree of crystallinity.[23,24] We corroborate this observation by the SEM images which we show in **Figure 1**, where we observed a highly faceted crystalline surface for x = 0.02 composition. With further increasing the PbI_2 concentration, we observe the XRD peak intensities to decreased with respect to the x = 0 analogue peak intensity and finally drop down to only a quarter of that of the x = 0 sample intensity, when $PbCl_2$ is completely replaced with PbI_2 (i.e. x = 1 in **Figure S1**). We also calculate the crystallites size and microstrain from the XRD patterns, which we present in **Figure 2b**. Line broadening, i.e. full width half maximum (FWHM) values of diffractions peaks, are commonly used to estimate the crystallite size in polycrystalline thin films and nanoscopic materials. However, apart from the crystallite size effect, microstrain originated from lattice imperfections structural defects including dislocations, stacking faults, twinning, and grain boundaries, can also induce line broadening.[25–28] We give a more detailed description of microstrain analysis in the SI, but briefly here, strain is extension (or compression) divided by original length, and microstrain is a result of local variations in the lattice constant throughout the crystalline material, induced by crystal imperfections. To evaluate the effects of size and microstrain discretely, we adopt Williamson-Hall analysis (**Figure S2**).[29] As compared to the x = 0 film, the crystallite size is

increased slightly with x = 0.02. With further increasing PbI_2 ratio, the crystallite size decreases. Looking at the microstrain, we determine that the microstrain remains low (0.15%, which means there is approximately 0.15% variation in the lattice constant throughout the film) for x = 0 and 0.02, but begins to increase with the increasing PbI_2 content, reaching 1% at x = 1. We note that the peak intensity in the x = 1 film is very weak, which many induce a relatively large error in the final microstrain value as compared to the other samples. Nevertheless, from the microstrain analysis, we can clearly see that excessive PbI_2 substitution increase the microstrain, consistent with an increased density of crystal defects, which will be unfavorable for the final device performance if these crystal defects are responsible for the creation of recombination sites. We note that there is currently ambiguity as to whether the apparent crystalline domains observed in SEM images, are truly single crystal domains, or if there is a nanoscale sub crystallinity within each domain. Resolving this issue is not central to our work here, but we do note that the crystal domain size which we determine from our XRD peak width fitting, is in the order of 100's nm. This is consistent with the scale of the grains which we observe in the SEM images.

In a quest to further understand the impact of varying the ratio of $PbCl_2$ to PbI_2, we studied the crystallization process in the perovskite films by performing optical microscopy measurements at different stages in the film fabrication. As we show in **Figure 3**, these images give a remarkably clear visualization of the multiple processes occurring during crystallization of the polycrystalline films. The crystallization process involves two main stages; crystal nucleation, or early time growth of individual crystallites, and then coarsening or growth of those crystals. In the neat PbI_2 precursor, x = 1, we observe the formation of brown-colored crystallites embedded within a light yellow/clear phase just after spinning and blow drying the precursor, and the brown-colored domains grown within this clear phase when heated at 60 ºC for 5 min. To elucidate the crystal structure of those early time crystallites we performed XRD of

perovskite films after annealed at 60 °C for 5 minutes (which we show **Figure S3**). We mainly assign the XRD pattern of this film as the $MAPbI_3$.[8,22] There are additional non-perovskite peaks at 2θ position of ~ 11°, which we have previously assigned to a "precursor phase" observable in a range of different perovskite processing routes which start from solutions of excess organic cation.[14,15] Here, we assign this precursor phase in the optical micrograph to being the yellow phase surrounding the brown perovskite crystallites.

Similarly, when we look at the as-cast film from the solutions containing neat $PbCl_2$ (x = 0) we observe both brown and yellow/clear phase throughout the film with flower-shaped morphology, as we show in **Figure 3a-1**. When we annealed the films at 60 °C for 5 minutes, the brown regions with perovskite appear to grow from within or around the periphery of these "precursor" regions. In the X-ray spectrum of this film (**Figure S3**), we observe peaks corresponding to $MAPbI_3$ and precursor phases at 2θ position of 14.2° and 14.7°, respectively.[22,30,31]

~~When we substitute 2 mol% of $PbCl_2$ with PbI_2 (i.e. x = 0.02), several distinctive regular quadrilateral-shaped dark brown colored crystals appeared within the uniform light-yellow background.~~ When we substitute 2 mol% of $PbCl_2$ with PbI_2 (i.e. x = 0.02), several distinctive regular quadrilateral-shaped dark brown colored crystals appeared within the uniform light-yellow background, as we show in **Figure 3a**. Notably, we do not observe such regularly-shaped domains in the films cast from the x = 0 and x = 1 solutions. In **Figure S4** we show high magnification optical microscope images using the darkfield illumination to highlight the morphological features. We can clearly observe a substructure within these large quadrilateral-shaped domains, consistent with them having formed from the conglomeration of smaller crystallites at very early stages during the film formation, rather having grown from a single seed. This also explains why we have much smaller apparent grain size, as inferred from SEM images and XRD broadening, in the final crystallised films, in comparison to these tens of micron size crystals. With the annealing of these x = 0.02 films at 60 °C for 5 minutes, we

observe that these crystals grow and coalesce by assimilating ions from within the background matrix. From the XRD pattern (**Figure S3**) of these x = 0.02 films (annealed at 60 °C for 5 min.), we observe the 2θ reflection which we assign to the precursor phase, at around 14.7°. The peak intensity at 14.2° (110) related to the $MAPbI_3$ formation for the films heated for 5 minutes at 60 °C is 8 times higher in the x = 0.02 film than that in the x =0 analogue, (we show the raw data in **Figure S3**). When we further increased the molar concentration of the PbI_2 to x = 0.05 and 0.4 in the precursor, instead of quadrilateral crystals, we observed large and less densely distributed star-shaped brown crystals in the as cast films. For x = 0.4, we observe cracks/holes in the center of these star-shaped crystals, indicating that they have formed via the agglomeration of several smaller crystals. In addition, as we shown in **Figure S3**, the $MAPbI_3$ peak intensity is dramatically decreased with the further increase of PbI_2 content in the precursor solution (i.e. x = 0.05 and 0.4). Hence, we interpret the enhanced XRD peak intensity in the x = 0.02 film to indicate an increase in perovskite crystallinity.[23]

We address the mechanism of crystallization from $3MAI:(1-x)PbCl_2:xPbI_2$ starting precursor: It is already known that the perovskite starting solutions are not simply dissolved ions, but a combination of dissolved ions, complexes and colloids, and that nano-scale coordination chemistry has an influence upon the thin film crystallization.[32,33] In **Figure S6** we show dynamic light scattering (DLS) on our perovskite precursor solutions (the same 38 wt% solutions as used for spin-coating) in order to determine the changes in colloid size and distributions. We do observe the intensity peak position shifts from large particles (for x = 0) to smaller particle size (for x = 1) as we substitute $PbCl_2$ with PbI_2. Additionally, the intensity peak width of x = 0.02 and 0.05 solutions is sharper than their x= 0 analogue. This indicates that varying PbI_2 content in the precursor composition does have an impact upon the size and uniform distribution of lead halide colloids/complexes in the precursor solution. On the basis of coordination chemistry, lead poly-iodide $[PbI_n]^{(n-2)}$ complex exists in the starting solution,

and they are likely to be central building blocks during perovskite crystallization.[33,34] In order to investigate the starting solutions further, in **Figure S5** we show UV-vis absorption spectra of the starting solutions, which we diluted to 6 mM solution so as to perform transmission spectroscopy. The $[PbI_n]^{(n-2)}$ complexes exhibit lower energy charge-transfer absorption bands for $[PbI_3]^-$ at 370 nm and for $[PbI_4]^{2-}$ at 425 nm.[34] In the UV-vis spectra, we observe an increasing of absorption band at 370 nm and 425 nm with increasing of PbI_2 content in the precursor solution, consistent with a small substitution of PbI_2 into the mixed halide precursor solution inducing $[PbI_n]^{(n-2)}$ complex formation.

Herein, we propose that the homogeneous distribution of perovskite crystallites at early times, and their subsequent growth, which we observe for the x = 0.02 samples, is related to the formation of small fraction $[PbI_n]^{(n-2)}$ in the precursor solution. When we look at the optical images for the x = 0.02 films, and consider the information from the XRD measurements, the nucleation and growth process is consistent with the colloids in solution being $[PbI_n]^{(n-2)}$ complexes which form $MAPbI_3$ nucleation crystals. Further heating then allows the $MAPbI_3$ crystals to grow, consuming the reservoir of ions from the yellow background i.e. an inherent mixed-halide precursor phase.

The perovskite film morphology and crystallinity has been repeatedly observed to have a significant impact upon the photo-physical properties of the material. In **Figure 4 a** and **b**, we show the absorption and emission spectra, and time resolved photoluminescence (PL) of two perovskite films fabricated on glass substrates from x = 0 and 0.02 solutions. Films cast from the x = 0.02 solution show a slight increase in UV-Vis absorbance, consistent with higher levels of crystallinity[16] and fewer pinholes,[16,35] and substantially higher PL intensity. We determine the corresponding PL quantum efficiency (PLQE) to be 9.12 ± 1.25% and 15.1 ± 1.02% for the films cast from the x = 0 and x = 0.02 samples respectively (which we measure by illuminating

the films with a 532 nm CW laser at 200 mW/cm^2 irradiance).[36,37] Consistent with the time-resolved PL, the higher PLQE value indicates a lower fraction of non-radiative decay pathways in the perovskite films. We show the time resolved PL of the corresponding films in **Figure 4 b.** By fitting PL decay dynamics on the perovskite film surface with our model[37,38], we estimate electron-hole recombination constant (γ) and concentration of traps (n_t), and we summarized the values in **Figure S7**. Interestingly, we estimate n_t on to be almost the same for both films, while we estimate the γ value to be an order of magnitude reduces from 1.02×10^{-9} cm^3 s^{-1} and 8.30×10^{-11} cm^3 s^{-1} for x = 0 and 0.02 films, respectively. In **Figure S8** we observe PL quenching behavior with both hole extracting Spiro-OMeTAD and electron extracting C_{60} on the perovskite films. We observe more efficient and faster PL quenching in the x = 0.02 film, which implies better charge extraction.

This confirms that the resulting films processed from the x = 0.02 precursor, not only yield superior thin film morphology and crystallographic features, but also result in higher optoelectronic quality of the perovskite material. We note that for further increments in the PbI_2 content in the precursor i.e. x = 0.05, 0.4 and 1, we observe a substantial deterioration in the photoluminescence lifetime and PLQE, which we show in **Figure S9**.

In order to assess the impact of the variations in perovskite film quality in complete solar cells, we fabricate and characterize planar hetero-junction solar cells in a controlled humidity air atmosphere. We employ the perovskite films with increasing PbI_2 content processed from the 3MAI:(1-x)$PbCl_2$:xPbI_2 solutions, sandwiched between a compact TiO_2 layer as the n-type electron collection layer, and 2,2(7,7(-tetrakis-(N,N-di-pmethoxyphenylamine)9,9(-spirobifluorene))) (spiro-OMeTAD) as the p-type hole collection layer, the results of which we show in **Figure S10**. As we expect from the photo-physical properties and morphological results, we observe that incorporation of 2 mol% (x = 0.02) PbI_2 in the perovskite starting solutions dramatically improves the device performance. However, further increasing the PbI_2

content leads to deterioration in the device performance. The solar cells we have just presented employ a compact TiO_2 layer as the n-type charge collection electrode. However, the interface between the compact TiO_2 and the perovskite film appears to amplify the current-voltage hysteresis, often observed in perovskite solar cells.[39] Here, to inhibit hysteresis in the solar cells, we include an additional layer of C_{60} on top of the TiO_2.[40–42] It is worth mentioning that the morphology of the perovskite films deposited on C_{60} coated TiO_2 substrates may be different with that on neat TiO_2 substrate. In **Figure S11**, we show the morphology of perovskite films deposited on C_{60} coated TiO_2 substrates. The x = 0 perovskite film displays slightly better surface coverage on C_{60} coated TiO_2 substrate compared with that on neat TiO_2 substrate. The morphology of the perovskite films coated on top of the TiO_2/C_{60} substrates, mainly improve film uniformity as we observe in **Figure S11 c** and **d** as compared to those films processed on the TiO_2 substrates when using different PbI_2 contents. In **Figure 5** we show current-density voltage (*JV*) curves for the best performing cells employing a compact TiO_2/C_{60} layer as the n-type electron collection layer[40,41] with x = 0 and x = 0.02 measured under simulated sun light (100 $mWcm^{-2}$, AM1.5). We determine the power conversion efficiency (and solar cell performance parameters) from the forward-bias to short-circuit (FB-SC) *JV* curves to be 19.1 % (J_{sc} = 23.1 mA cm^{-2}, V_{oc} = 1.08 V, and *FF* = 0.77) for the cell fabricated with 2 mol% PbI_2 (x = 0.02), in comparison to 16.8 % (J_{sc} = 20.7 mA cm^{-2}, V_{oc} of 1.07 V, and *FF* = 0.77) for the devices incorporating the x = 0 perovskite films. We show the external quantum efficiency (EQE) spectra for typical device for each films in **Figure S12**. The same trend which we observe form the measured *JV* curves, is replicated in the EQE spectra, consistent with the enhanced photocurrent from the x = 0.02 films. The integrated J_{sc} from the EQE over the solar spectrum from 400 nm to 900 nm wavelength gives an estimated J_{sc} of 17.4 and 20.2 $mAcm^{-2}$ for the x = 0 and 0.02 devices, respectively. The J_{sc} value we measured under the solar simulator for these precise devices was 20.2 and 22.3 mA cm^{-2} respectively. Our EQE set up is not sensitive below 400 nm due to an optical filter in place, whereas the solar simulator

does have a component below 400 nm which contributes ~ 1 $mAcm^{-2}$ additional photocurrent current (as is the case under real sun light). The further discrepancy of ~1 $mAcm^{-2}$ is within the measurement accuracy. In Table 1, we show the average device performance of 30 devices for each composition, showing the parameters determined from both forward-bias to short-circuit (FB-SC) and short-circuit to forward-bias (SC-FB) current-voltage sweeps. We show the JV curves of typical device from both sweeps in **Figure S13**. We observe that the average value of the power conversion efficiency, determined from the FB-SC *JV* scans, for the device incorporating the x = 0.02 perovskite films, shows a relative improvement of 20%, as compared to those devices fabricated from the x = 0 solution. Additionally, we observe that the standard deviation of each performance parameters for the "x = 0.02" devices, is smaller than that of the devices fabricated with no PbI_2 in the starting solution, indicating improved reproducibility. The current-voltage hysteresis still persists for all devices, therefore in order to determine the actual steady-state stabilized power conversion efficiency of devices, we performed a "stabilized power output" (SPO) measurement by measuring the photocurrent density over time at a fixed voltage at the maximum power point which we determined from the FB−SC *JV* curves (Figure 5b). We find that the efficiency and photocurrent for the devices fabricated from the x = 0 solution stabilize at 15.5 % and 17.5 $mAcm^{-2}$ (at 0.89 V) respectively. We observe further improvement in the parameters for the devices fabricated from x = 0.02 precursor, with efficiency and current density values stabilizing at 17.2 % and 19.9 mA/cm^2 (at 0.87V), respectively.

3. Conclusion

We have demonstrated that the presence of a small amount of PbI_2 in the mixed-halide precursor (3MAI:$PbCl_2$) has a profound impact upon the crystallization process and on the as crystallized film morphology and electronic properties of the perovskite thin films. With the

substitution of a small fraction (i.e. 2 mol%) of $PbCl_2$ with PbI_2, during thin film formation we create a relatively homogeneous density of $MAPbI_3$ "seed" crystals, within a homogeneous matrix of a mixed halide precursor phase. Crystallization under temperature leads to uniform growth of these crystals into highly crystalline thin-films with visibly faceted and orientated grain morphology. We have shown that these "structurally improved" films, exhibit enhanced optoelectronic properties, and resultantly deliver improved solar cell performance when integrated into complete devices. Our best planar heterojunction cell deliver a *JV* measured power conversion efficiency of 19.1% and a stabilized power output of 17.2%.

4. Experimental Section

Perovskite films and device fabrication

FTO-coated glass sheets (TEC 7, 7Ω/sheet, Pilkington) were etched with zinc powder and 2M HCl to obtain the required electrode pattern. The sheets were then washed with 2% Hellmanex in water, deionized water, acetone, ethanol and iso-propanol. The last traces of organic residues were removed by oxygen plasma cleaning for 10 min. For the only TiO_2 compact layer devices, the FTO sheets were coated titanium sol precursor at 2000 rpm for 1 min by spin coating. The titanium sol precursor was prepared by drop wise adding a solution of 175 µL of tetra-titaniumisopropoxide (Aldrich) in 1.25 mL of ethanol into a solution of 17.5 µL of Aquarius HCl solution (2M) in 1.25 mL of ethanol. TiO_2 coated FTO substrate was then heated to 150°C for 10 min and 300 °C for 20 min then ramp up to 500 °C for 20 min. For the optimized device structure, the FTO sheets were subsequently coated with a TiO_2 compact layer by chemical bath deposition with 40 mM aquarius $TiCl_4$ solution at 70°C for 60 min. The TiO_2 compact layer was heated at 450 °C for 30 min. C60 (10 mg/ml in 1,2, di-chlorobenzene, Aldrich) layers were coated on TiO_2 compact layers at 3000 rpm for 30 sec. 38wt% perovskite precursor solutions were made by 3 molar of CH_3NH_3I (MAI: Dyesol), 1-x molar of $PbCl_2$ (98%, Aldrich) and x

molar of PbI_2 (99%, Aldrich) dissolving in dimethylformamide (dehydrate DMF; Aldrich). The Pb^{2+} concentration was fixed for all perovskite precursors. Each perovskite precursor solution was coated onto the TiO_2 compact layer or the TiO_2/C60 by a consecutive two-step spin-coating process at 1300 rpm for 25 sec and 3000 rpm for 15 under low humidity (15-20% at 20°C) condition with a dry compressed air parch in dry box. The perovskite films were quickly dried by the compressed air blowing for 30 sec. The perovskite films were drying at 20 °C for 15 min and then 70 °C for 15 min on the hot plate. The dried films were annealing at 100 °C for 90 min then ramp up to 120 °C for 10 min in the box oven without controlling humidity. 3MAI:PbI_2 were annealing at 150 °C for 10 min on final annealing process to evaporate excess MAI. 96 mg 2,2(7,7(-tetrakis-(N,N-di-pmethoxyphenylamine)9,9(-spirobifluorene))) (spiro-OMeTAD) was solved in 1 ml cholobenzene with additives of 15 µl tert-butylpyridine and 35 µl lithium bis(trifluoromethylsulfonyl)imide salt in acetonitrile (170 mg ml^{-1}). 100 nm of Ag metal contact layer was deposited as the counter electrode on the HTM layer by thermal evaporation.

Characterization

A scanning electron microscope (SEM; Hitachi, S-4300) and an optical microscope (OM; Sonic, BS D8000II and Nikon ECLIPSE LV100N POL) were used to acquire SEM and OM images, and the perovskite films were made on the TiO_2/FTO substrate. For X-ray diffraction (XRD) and photo-physical property measurement were carried out on the TiO_2/FTO substrate. XRD patterns were obtained using a Panalytical X'Pert Pro x-ray diffract meter. For the photo-physical properties, the perovskite films were made on the glass substrate. UV-vis absorption spectra were measured by a commercial spectrophotometer (Varian Cary 300 UV-Vis, USA). Steady-state PL and time-resolved PL measurement were obtained with Fluorescence Lifetime Spectrometer (Fluo Time 300, PicoQuant FmbH). Perovskite films were exited using a 507 nm laser pulsed at frequencies between 0.2 - 10 MHz. Quantum efficiency (PLQE) values were

determined using a 532nm CW laser excitation source (Suwtech LDC-800) to illuminate a sample in an integrating sphere (Oriel Instruments 70682NS), and the laser scatter and PL collected using a fiber-coupled detector (Ocean Optics USB 2000+). PLQE calculations were carried out using established techniques. The laser intensity was adjusted using optical density filters. The cell performance evaluated by the current–voltage (J-V) measurements under simulated solar light (AAB ABET technologies Sun 2000 solar simulator) with its light intensity, 100.6 ± 0.6 mW cm^{-2} (AM 1.5), calibrated against a standard amorphous-silicon PV cell (NREL-calibrated KG5 filtered silicon reference cell). The mismatch factor was estimated to be M=1.035405 and the lamp intensity changes to account for this mismatch. The J-V curves were measured by short circuit (0V) to forward bias (1.4V) and forward bias (1.4V) to short circuit (0V). The cell aperture area of light incidence was set to 0.0913 cm^2photoactive area by employing an opaque mask. The "stabilized power output" of the devices versus time was measured under load near the maximum power point at the same conditions.

Supporting Information

Supporting Information is available from the Wiley Online Library or from the author.

Acknowledgements

The research leading to these results has received funding from the European Union Seventh Framework Program (FP7/2007–2013) under grant agreement no. 604032 of the MESO project. The authors would like to thank Dr Hsin-Wei Chen and Dr Tsutomu Miyasaka in Toin University of Yokohama for supporting to take optical microscopic images, and Dr Michael B. Johnston and Jay B. Patel for assistance with EQE measurements.

Received: ((will be filled in by the editorial staff))
Revised: ((will be filled in by the editorial staff))
Published online: ((will be filled in by the editorial staff))

[1] P. Docampo, J. M. Ball, M. Darwich, G. E. Eperon, H. J. Snaith, *Nat. Commun.* **2013**, *4*, 2761.

[2] M. Kaltenbrunner, G. Adam, E. D. Głowacki, M. Drack, R. Schwödiauer, L. Leonat, D. H. Apaydin, H. Groiss, M. C. Scharber, M. S. White, N. S. Sariciftci, S. Bauer, *Nat. Mater.* **2015**, *14*, 1032.

[3] J. S. Yang, Woon Seok, Jun Hong Noh, Nam Joong Jeon, Young Chan Kim, Seungchan Ryu, S. Il Seok, *Science.* **2015**, 1.
[4] M. Saliba, T. Matsui, J.-Y. Seo, K. Domanski, J.-P. Correa-Baena, N. Mohammad K., S. M. Zakeeruddin, W. Tress, A. Abate, A. Hagfeldt, M. Grätzel, *Energy Environ. Sci.* **2016**, 2016, *9*, 1989-1997.
[5] D. Bi, W. Tress, M. I. Dar, P. Gao, J. Luo, C. Renevier, K. Schenk, A. Abate, F. Giordano, J.-P. Correa Baena, J.-D. Decoppet, S. M. Zakeeruddin, M. K. Nazeeruddin, M. Gra tzel, A. Hagfeldt, *Sci. Adv.* **2016**, *2*, e1501170.
[6] N. J. Jeon, J. H. Noh, Y. C. Kim, W. S. Yang, S. Ryu, S. Il Seok, *Nat. Mater.* **2014**, 1.
[7] M. Xiao, F. Huang, W. Huang, Y. Dkhissi, Y. Zhu, J. Etheridge, A. Gray-Weale, U. Bach, Y.-B. Cheng, L. Spiccia, *Angew. Chemie* **2014**, *126*, 10056.
[8] N. Sakai, S. Pathak, H.-W. Chen, A. A. Haghighirad, S. D. Stranks, T. Miyasaka, H. J. Snaith, *J. Mater. Chem. A* **2016**, *4*, 4464.
[9] K. Hwang, Y. S. Jung, Y. J. Heo, F. H. Scholes, S. E. Watkins, J. Subbiah, D. J. Jones, D. Y. Kim, D. Vak, *Adv. Mater.* **2015**, *27*, 1241.
[10] D. Vak, K. Hwang, A. Faulks, Y. S. Jung, N. Clark, D. Y. Kim, G. J. Wilson, S. E. Watkins, *Adv. Energy Mater.* **2015**, *5*, 1.
[11] Z. Wei, H. Chen, K. Yan, S. Yang, *Angew. Chemie - Int. Ed.* **2014**, *53*, 13239.
[12] Y. Deng, E. Peng, Y. Shao, Z. Xiao, Q. Dong, J. Huang, *Energy Environ. Sci.* **2015**, *8*, 1544.
[13] K. W. Tan, D. T. Moore, M. Saliba, H. Sai, L. a Estroff, T. Hanrath, H. J. Snaith, U. Wiesner, *ACS Nano* **2014**, *8*, 4730.
[14] D. T. Moore, H. Sai, K. W. Tan, D.-M. Smilgies, W. Zhang, H. J. Snaith, U. Wiesner, L. a. Estroff, *J. Am. Chem. Soc.* **2015**, *137*, 2350.
[15] W. Zhang, M. Saliba, D. T. Moore, S. Pathak, M. Horantner, T. Stergiopoulos, S. D. Stranks, G. E. Eperon, J. a Alexander-Webber, A. Abate, A. Sadhanala, S. Yao, Y. Chen, R. H. Friend, L. a Estroff, U. Wiesner, H. J. Snaith, *Nat. Commun.* **2014**, *6*, 6142.
[16] G. Grancini, A. R. Srimath Kandada, J. M. Frost, A. J. Barker, M. De Bastiani, M. Gandini, S. Marras, G. Lanzani, A. Walsh, A. Petrozza, *Nat. Photonics* **2015**, *9*, 695.
[17] D. W. DeQuilettes, S. M. Vorpahl, S. D. Stranks, H. Nagaoka, G. E. Eperon, M. E. Ziffer, H. J. Snaith, D. S. Ginger., *Science.* **2015**, *348*, 683.
[18] G. Grancini, S. Marras, M. Prato, C. Giannini, C. Quarti, F. De Angelis, M. De Bastiani, G. E. Eperon, H. J. Snaith, L. Manna, A. Petrozza, *J. Phys. Chem. Lett.* **2014**, *5*, 3836.
[19] C. Roldan-Carmona, P. Gratia, I. Zimmermann, G. Grancini, P. Gao, M. Graetzel, M. K. Nazeeruddin, *Energy Environ. Sci.* **2015**, *8*, 3550.
[20] Q. Chen, H. Zhou, T. Song, S. Luo, Z. Hong, *Nano Lett.* **2014**, *14*, 4158.
[21] F. Huang, Y. Dkhissi, W. Huang, M. Xiao, I. Benesperi, S. Rubanov, Y. Zhu, X. Lin, L. Jiang, Y. Zhou, A. Gray-Weale, J. Etheridge, C. R. McNeill, R. a. Caruso, U. Bach, L. Spiccia, Y.-B. Cheng, *Nano Energy* **2014**, *10*, 10.
[22] T. Baikie, Y. Fang, J. M. Kadro, M. Schreyer, F. Wei, S. G. Mhaisalkar, M. Gratzel, T. J. White, *J. Mater. Chem. A* **2013**, *1*, 5628.
[23] S. Pathak, A. Sepe, A. Sadhanala, F. Deschler, A. Haghighirad, N. Sakai, K. C. Goedel, S. D. Stranks, N. Noel, M. Price, S. Hu, N. A. Hawkins, R. H. Friend, U. Steiner, H. J. Snaith, *ACS Nano* **2015**, *9*, 2311.
[24] Y.-C. Huang, C.-S. Tsao, Y.-J. Cho, K.-C. Chen, K.-M. Chiang, S.-Y. Hsiao, C.-W. Chen, C.-J. Su, U.-S. Jeng, H.-W. Lin, *Sci. Rep.* **2015**, *5*, 13657.
[25] T. Ungár, *J. Mater. Sci.* **2007**, *42*, 1584.
[26] C. L. Tracy, M. Lang, J. M. Pray, F. Zhang, D. Popov, C. Park, C. Trautmann, M. Bender, D. Severin, V. a. Skuratov, R. C. Ewing, *Nat. Commun.* **2015**, *6*, 6133.

[27] A. Pramanick, X. P. Wang, C. Hoffmann, S. O. Diallo, M. R. V. Jørgensen, X.-L. Wang, *Phys. Rev. B* **2015**, *92*, 174103.
[28] I. Robinson, R. Harder, *Nat. Mater.* **2009**, *8*, 291.
[29] G. . Williamson, W. . Hall, *Acta Metall.* **1953**, *1*, 22.
[30] T. Baikie, N. S. Barrow, Y. Fang, P. J. Keenan, P. R. Slater, R. O. Piltz, M. Gutmann, S. G. Mhaisalkar, T. J. White, *J. Mater. Chem. A* **2015**, *3*, 9298.
[31] E. L. Unger, A. R. Bowring, C. J. Tassone, V. Pool, A. Gold-Parker, R. Cheacharoen, K. H. Stone, E. T. Hoke, M. F. Toney, M. D. McGehee, *Chem. Mater.* **2014**, *26*, 7158−7165.
[32] Y. Tidhar, E. Edri, H. Weissman, D. Zohar, G. Hodes, D. Cahen, B. Rybtchinski, S. Kirmayer, *J Am Chem Soc* **2014**, *136*, 13249.
[33] K. Yan, M. Long, T. Zhang, Z. Wei, H. Chen, S. Yang, J. Xu, *J. Am. Chem. Soc.* **2015**, *137*, 4460.
[34] K. G. Stamplecoskie, J. S. Manser, P. V. Kamat, *Energy Environ. Sci.* **2015**, *8*, 208.
[35] G. E. Eperon, V. M. Burlakov, A. Goriely, H. J. Snaith, *ACS Nano* **2014**, *8*, 591.
[36] J. C. de Mello, H. F. Wittmannn, R. H. Friend, *Adv. Mater.* **1997**, *9*, 230.
[37] S. D. Stranks, V. M. Burlakov, T. Leijtens, J. M. Ball, A. Goriely, H. J. Snaith, *Phys. Rev. Appl.* **2014**, *2*, 1.
[38] W. Zhang, S. Pathak, N. Sakai, T. Stergiopoulos, P. K. Nayak, N. K. Noel, A. A. Haghighirad, V. M. Burlakov, D. W. deQuilettes, A. Sadhanala, W. Li, L. Wang, D. S. Ginger, R. H. Friend, H. J. Snaith, *Nat. Commun.* **2015**, *6*, 10030.
[39] H. J. Snaith, A. Abate, J. M. Ball, G. E. Eperon, T. Leijtens, N. K. Noel, S. D. Stranks, J. T.-W. Wang, K. Wojciechowski, W. Zhang, *J. Phys. Chem. Lett.* **2014**, *5*, 1511−1515.
[40] K. Wojciechowski, S. D. Stranks, A. Abate, G. Sadoughi, A. Sadhanala, N. Kopidakis, G. Rumbles, C. Li, R. H. Friend, A. K. Jen, H. J. Snaith, *ACS Nano* **2014**, *8*, 12701.
[41] K. Wojciechowski, T. Leijtens, S. Siprova, C. Schlueter, M. T. Hörantner, J. T.-W. Wang, C.-Z. Li, A. K.-Y. Jen, T.-L. Lee, H. J. Snaith, *J. Phys. Chem. Lett.* **2015**, *6*, 2399.
[42] C. Tao, S. Neutzner, L. Colella, S. Marras, A. Ram, S. Kandada, M. Gandini, M. De Bastiani, G. Pace, L. Manna, M. Caironi, C. Bertarelli, A. Petrozza, *Energy Environ. Sci. Energy Environ. Sci* **2015**, *8*, 2365.

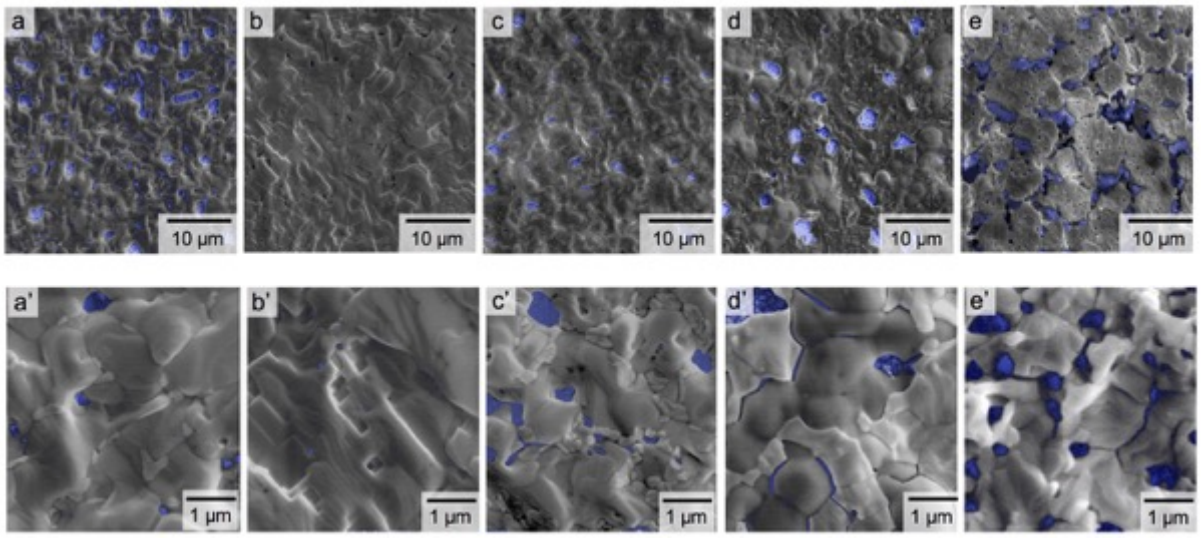

Figure 1. SEM images of the perovskite films deposited from precursor solutions containing 3MAI:(1-x)$PbCl_2$:xPbI_2, while varying the PbI_2 content with (a) x = 0 (b) 0.02, (c) 0.05, (d) 0.4 and (e) 1. SEM images on the bottom row show higher magnification of the same image shown on the top row. The uncovered area with perovskite thin film are marked as a false blue color to aid the reader.

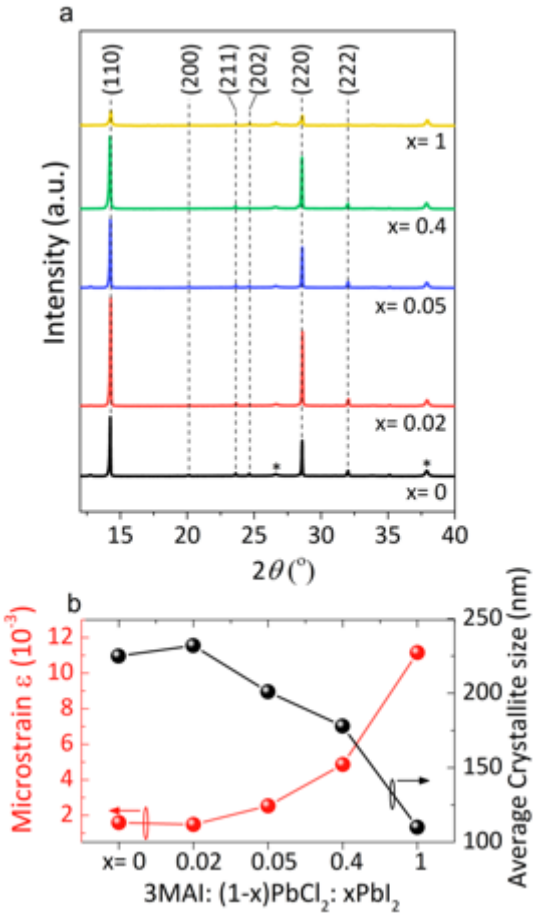

Figure 2. a) XRD patterns of the perovskite films deposited from precursor 3MAI:(1-x)$PbCl_2$:xPbI_2, while varying the PbI_2 content with x = 0, 0.02, 0.05, 0.4 and 1. * denotes the diffraction peaks from the FTO glass. b) Calculated microstrain and average crystallite size determined from XRD patterns by performing Williamson-Hall analysis.

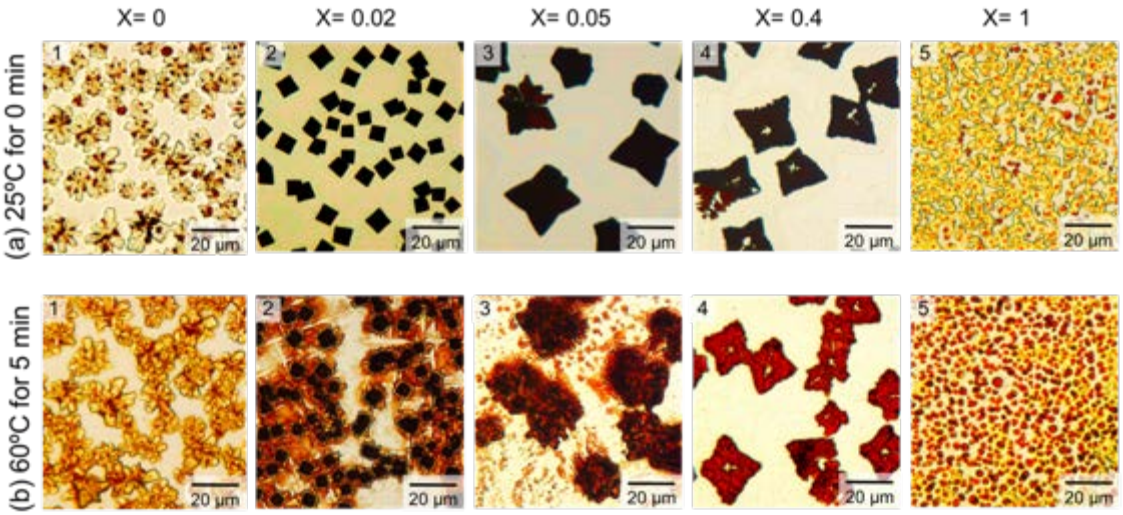

Figure 3. Optical micrographs taken during thermal annealing (a and b) for the perovskite films deposited from solutions of 3MAI:(1-x)$PbCl_2$:xPbI_2 in DMF, while varying the PbI_2 content with x = 0, 0.02, 0.05, 0.4 and 1.

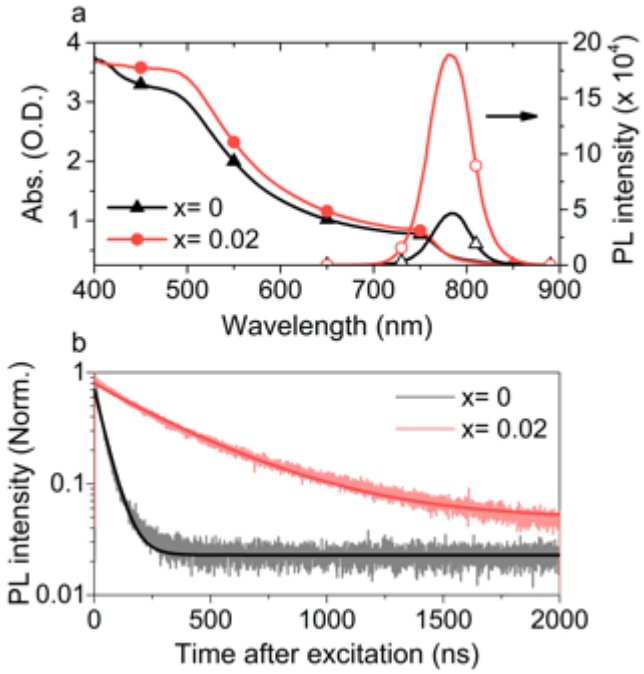

Figure 4 Photo-physical properties (a; UV-vis absorption, b; steady-state PL and c; time-resolved PL) of the perovskite films fabricated from 3MAI:(1-x)$PbCl_2$:xPbI_2. For the time resolved PL the samples were excited with 507 nm at 30 μJ/cm^2 per pulse. Thick lines are the model fits.

1

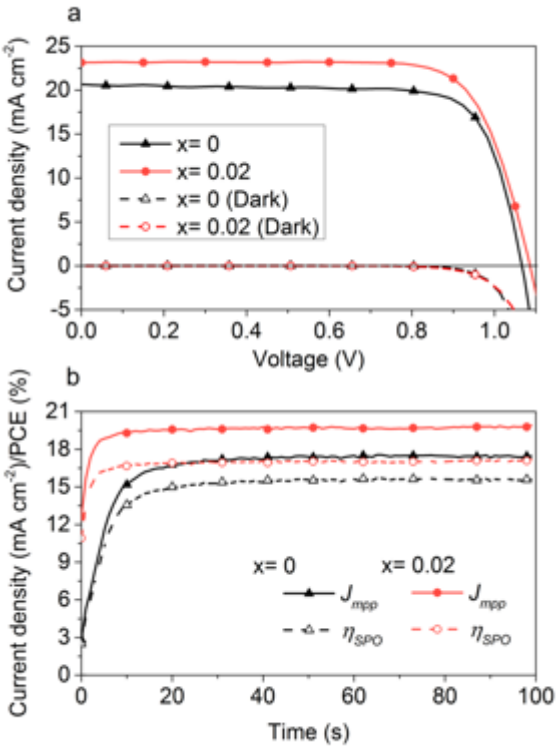
a
Current density (mA cm^{-2})
Voltage (V)
x= 0
x= 0.02
x= 0 (Dark)
x= 0.02 (Dark)
b
Current density (mA cm^{-2})/PCE (%)
Time (s)
x= 0
x= 0.02
J_{mpp}
η_{SPO}

Figure 5. (a) *JV* curves for the optimized perovskite solar cells, fabricated from 3MAI:$PbCl_2$ (x = 0), and 3MAI:0.98$PbCl_2$:0.02PbI_2 (x = 0.02) starting solutions. (b) Stabilized power output (SPO) and photocurrent density for the respective perovskite solar cells at the fixed maximum power point voltage (J_{mpp}). The devices performances were recorded under 1 sun illumination (100.9 $mWcm^{-2}$, AM1.5)

Table 1 Performance parameters for perovskite solar cells with the different perovskite precursors. Each value from JV sans and SPO measurements are the average of data taken from 30 and 15 devices, respectively

	Scan direction	J_{sc} *(mA cm^{-2})*	V_{oc} *(V)*	*FF*	*PCE (%)*	SPO (%)
x=0	*FB→SC*	21.3 ± 1.20	1.00 ± 0.09	0.67 ± 0.09	13.9 ± 2.02	11.1 ± 2.5
	SC→FB	21.1 ± 1.20	0.85 ± 0.18	0.49 ± 0.2	8.43 ± 2.60	
x= 0.02	*FB→SC*	22.2 ± 0.80	1.05 ± 0.03	0.70 ± 0.05	16.3 ± 1.53	15.4 ± 1.0
	SC→FB	22.1 ± 0.88	0.97 ± 0.04	0.51 ± 0.09	10.7 ± 1.58	

TOC

A fractional substitution of PbI_2 in the mixed-halide precursor (3MAI:$PbCl_2$) has a profound impact upon the crystallization process and on the as crystallized film morphology and electronic properties. The “structurally improved” film deliver a JV measured power conversion efficiency of 19.1%

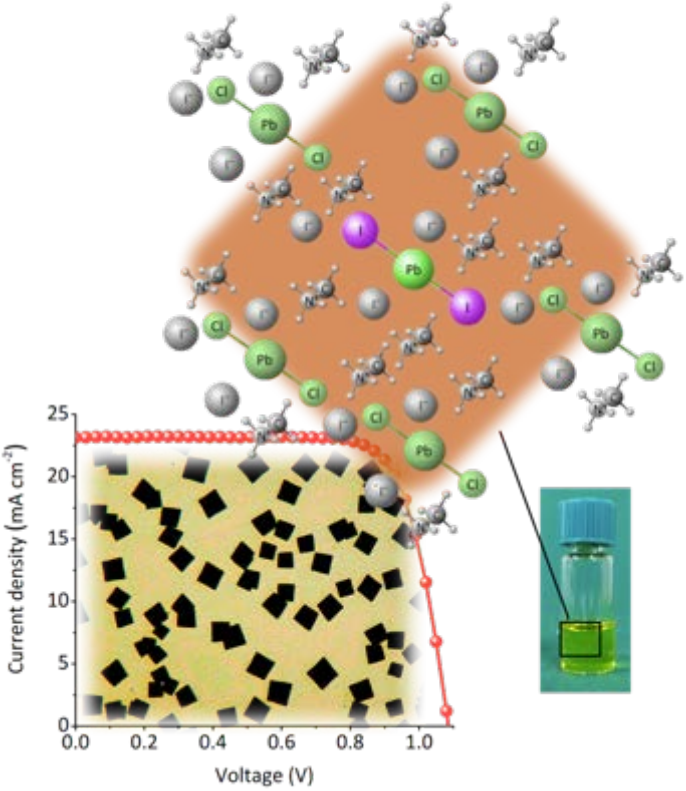

Supporting Information

Controlling Nucleation and Growth of Metal Halide Perovskite Thin-films for High Efficiency Perovskite Solar Cells

Nobuya Sakai, Zhiping Wang, Victor M Burlakov, Jongchul Lim, David McMeekin , Sandeep Pathak, and Henry J. Snaith[*]

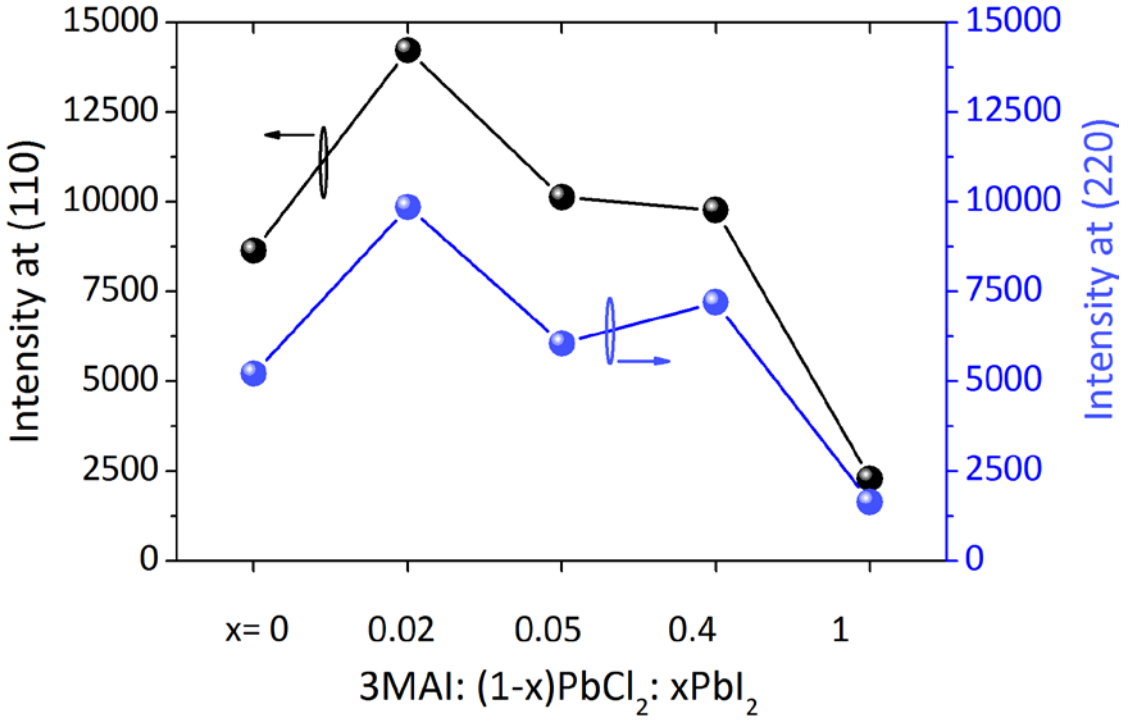

Figure S1. XRD intensities at (110) and (220) of the perovskite films deposited from precursor 3MAI:(1-x)$PbCl_2$:xPbI_2, while varying the PbI_2 content with x= 0, 0.02, 0.05, 0.4 and 1.

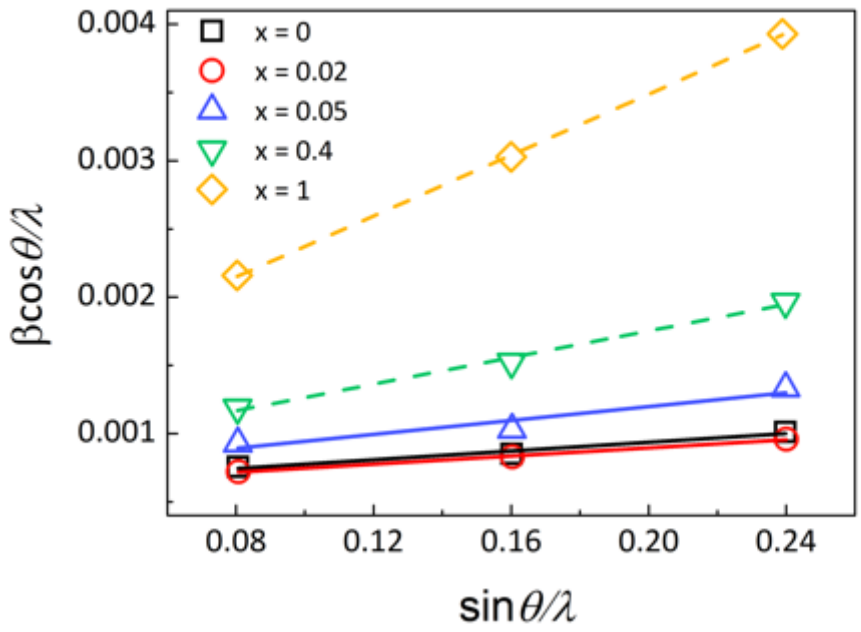

Figure S2 Williamson-Hall analysis of the perovskite films fabricated from 3MAI:(1-x)$PbCl_2$:xPbI_2

Williamson-Hall analysis

The broadening and shifts in the XRD peak maybe due to either the reduction in the grain size (Scherrer broadening) and/or non-uniform strain (microstrain). Strain is the relative change in size of an object with respect to its ideal size (or size before experiencing an external force). The microstrain in a crystalline material is a result of small fluctuations in the lattice spacing, induced by crystal imperfections/structural defects including dislocations, vacancies, stacking faults, interstitials, twinning, and grain boundaries.[43,44] By simply considering Braggs law for scattering, $n\lambda = 2d\sin\theta$, it is clear that small fluctuations in d (i.e. Δd) will result in small fluctuations, or broadening, in θ when measuring the X-ray diffraction from the material. We quantify the extent of microstrain in our perovskite films by analysing the peak broadening in the diffraction patterns according to the Williamson-Hall method.[45] This method uses the broadening of all peaks, expressed as integral breadths, were measured and instrumental broadening was subtracted to obtain the radiation-induced X-ray line broadening (the increase

in integral breadth relative to the intrinsic instrumental peak breadth). The angular dependences of these peak breadths (β_{hkl}) were fit using a convolution of the models for instrument (β_{ins}), crystallite size (β_{size}) and strain (β_{strain}) broadening:

$$\beta_{hkl} = \beta_{ins} + \beta_{size} + \beta_{strain} \quad (1)$$

As is shown in many studies, the β_{strain} and β_{size} are expressed by the equations:

$$\beta_{strain} = 4\varepsilon \tan\theta \quad (2)$$

$$\beta_{size} = \frac{K\lambda}{D\cos\theta} \quad (3)$$

where ε is the microstrain, θ is the diffraction angle of a given peak, λ is the X-ray wavelength, K is shape factor (i.e., 0.9) and D is the mean crystallite size. On rearranging the equation (1) we obtain,

$$\beta_{hkl} - \beta_{ins} = 4\varepsilon \tan\theta + \frac{K\lambda}{D\cos\theta} \quad (4)$$

i.e.,

$$\frac{\beta\cos\theta}{\lambda} = 4\varepsilon\frac{\sin\theta}{\lambda} + \frac{K}{D} \quad (5)$$

where β is the peak breadth after correction for instrumental broadening, i.e. $\beta_{hkl} - \beta_{ins}$, for brevity. Therefore, the Williamson-Hall plot can be constructed by plotting $\beta\cos\theta/\lambda$ against $\sin\theta/\lambda$.

The strain is then obtained from the slope (= 4ε) and the crystallite size (Å) is obtained from the intercept (= $\frac{K}{D}$).

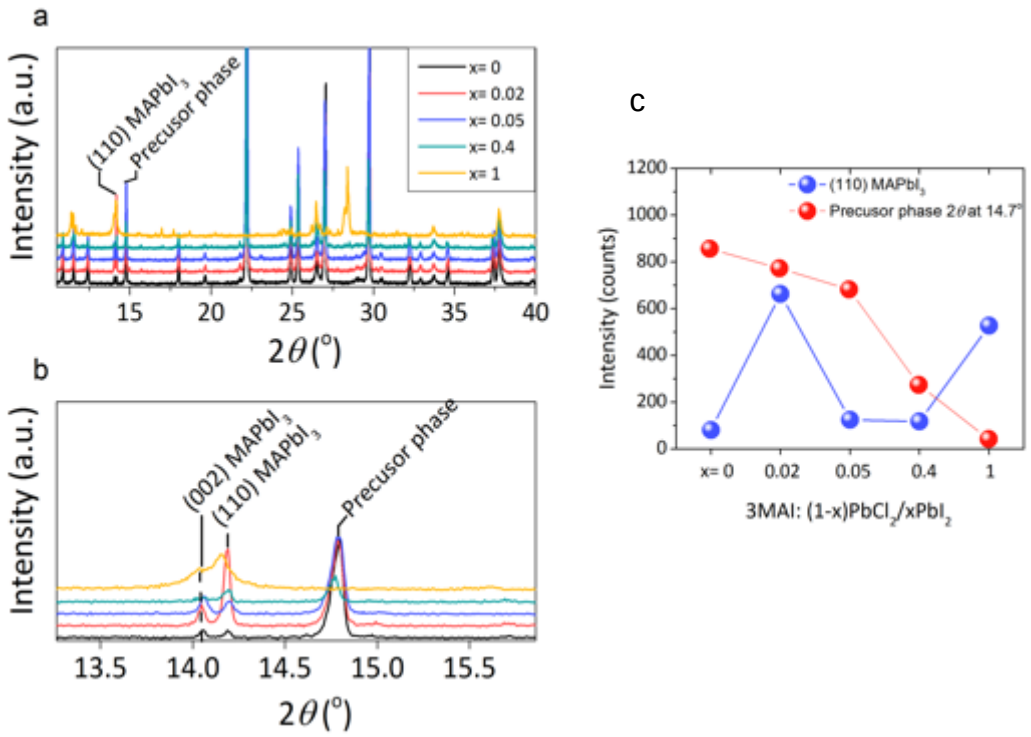

Figure S3. (a) X-ray diffraction patterns (XRD) for the post-dried perovskite films at 60 °C for 5 min fabricated from 3MAI:(1-x)$PbCl_2$:xPbI_2. The top of perovskite films was coated with PMMA (40mg/ml) in toluene. (b), Zoomed in X-ray reflections range at 2θ = 13 °to 16°. (c) Peak intensities of XRD patternat 14.2° and 14.7° may relate to (110) in $MAPbI_3$ and "precursor phase".

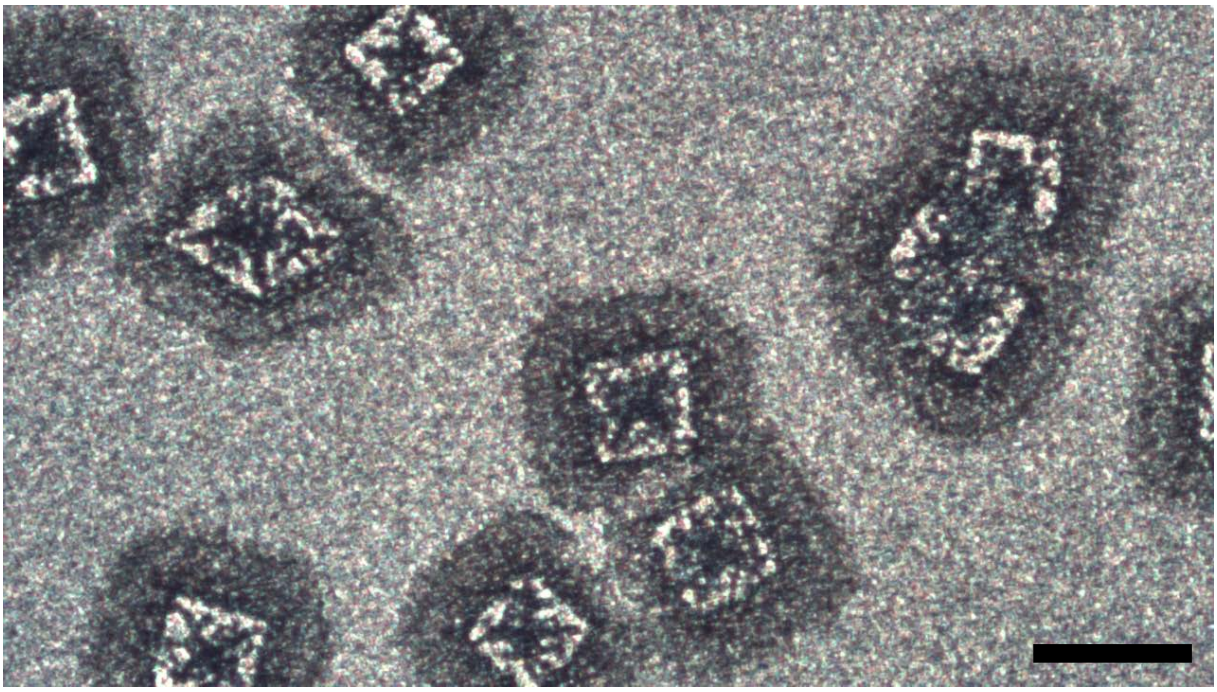

Figure S4. Optical micrograph taken of as cast film of the perovskite deposited from a solution of 3MAI:0.98$PbCl_2$:0.02 PbI_2 in DMF. The scale bar in this figure is 5 μm.

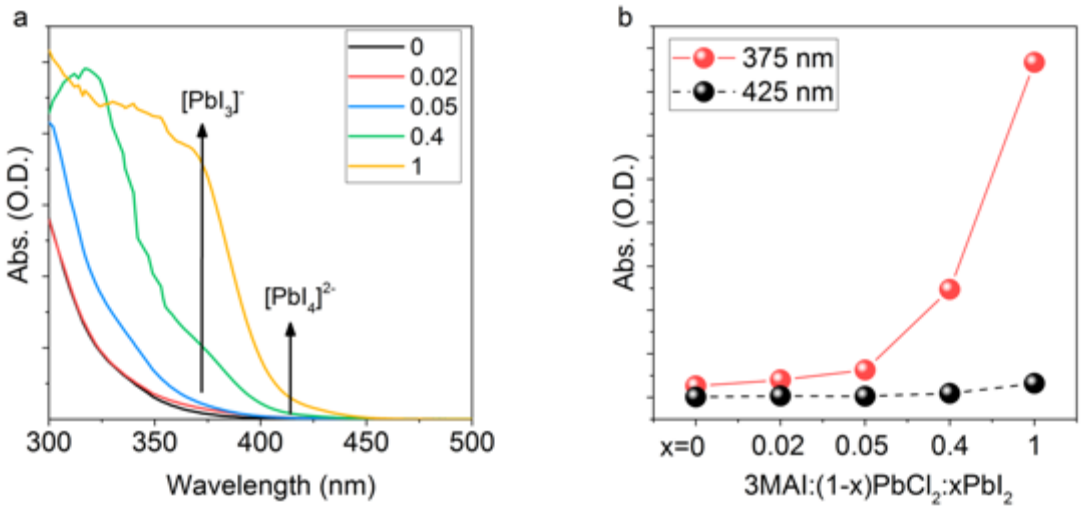

Figure S5. (a) UV-vis absorption of the perovskite precursor solution, which we diluted to 6 mM. (b) Absorption values at 375 nm and 425 nm of the 3MAI:(1-x)$PbCl_2$:xPbI_2 precursor solution, while varying the PbI_2 content with x= 0, 0.02, 0.05, 0.4 and 1.

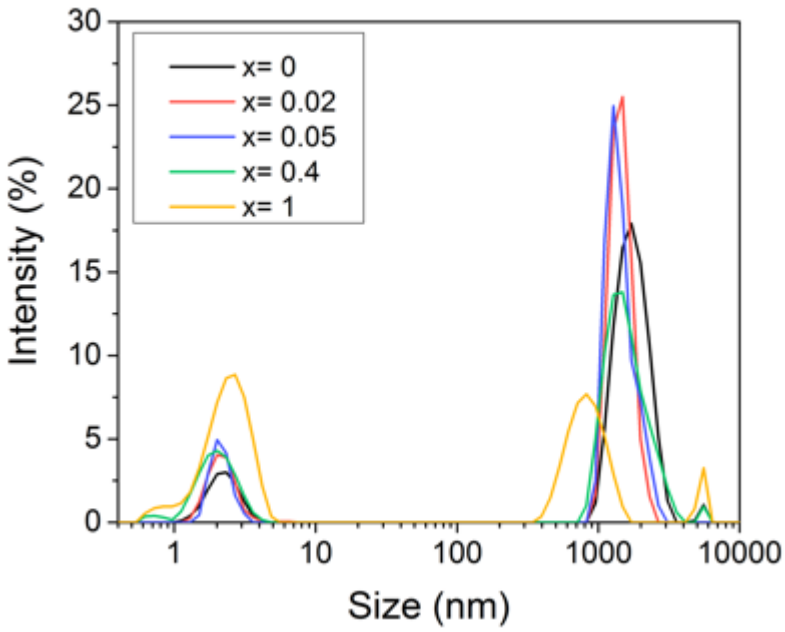

Figure S6. Dynamic Light Scattering measurement spectra of the perovskite precursors with different PbI_2 concentration into the formulation of $3MAI(1-x)PbCl_2:xPbI_2$.

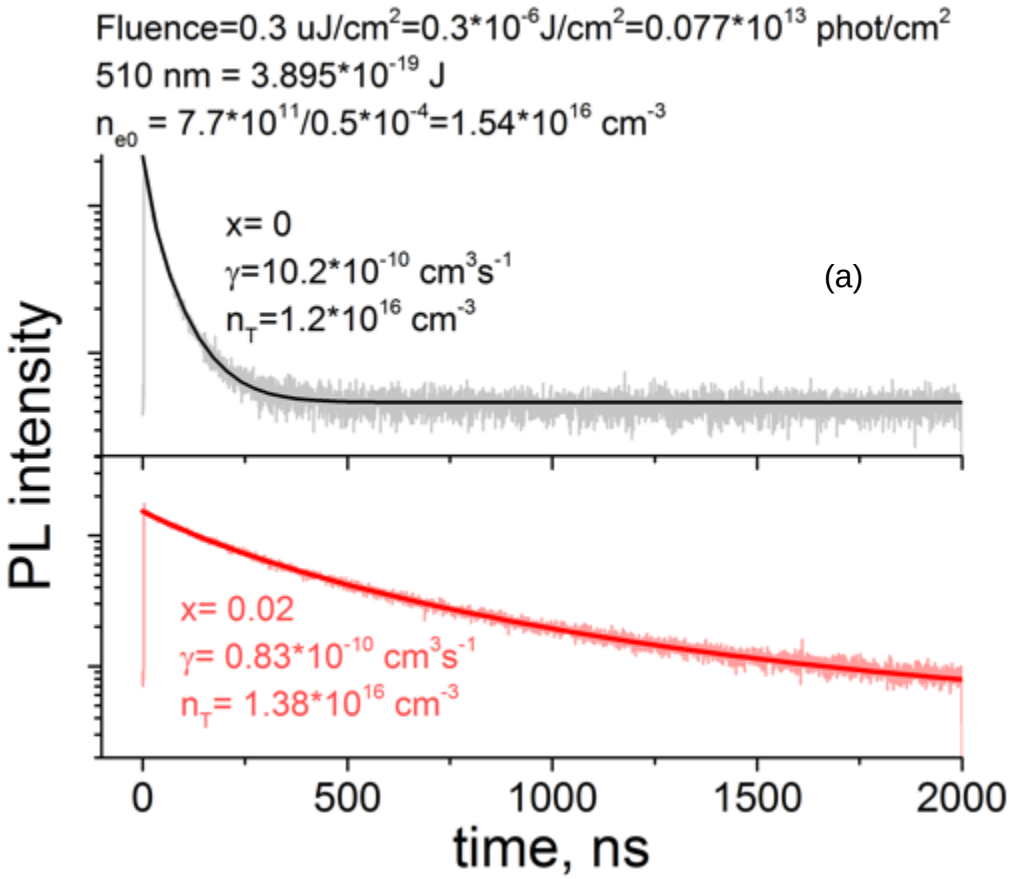

Figure S7. TRPL decay of the perovskite film fabricated from (a) 3MAI:$PbCl_2$ (x=0), and (b) 3MAI:0.98$PbCl_2$:0.02PbI_2(x=0.02)starting solutions with fitting result by our model.

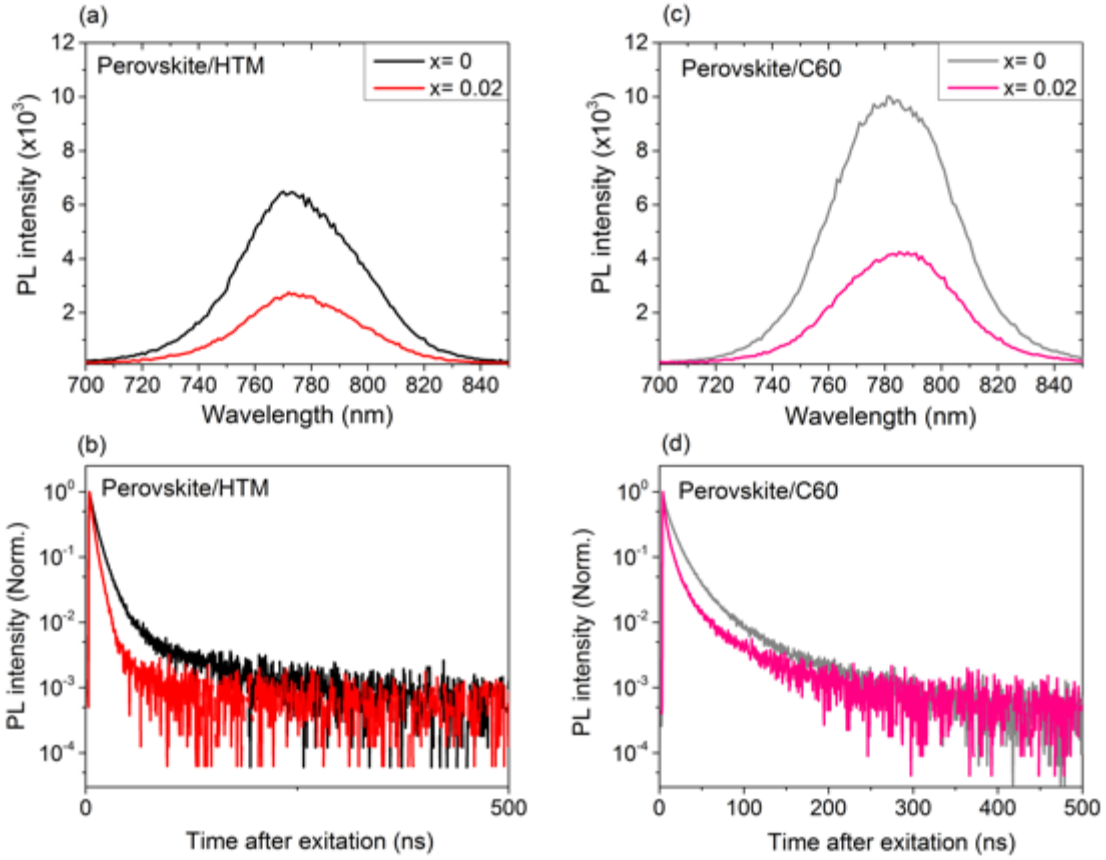

Figure S8. (a) Steady-state photoluminescence spectra of the perovskite film with hole-transport material (Spiro-OMeTAD) as *p*-type quencher and (c) electron-transport material (C60) as *n*-type quencher processed in a bi-layer configuration. (b) Time-resolved photoluminescence spectra of the perovskite film with Spiro-OMeTAD and (d) C60.

1

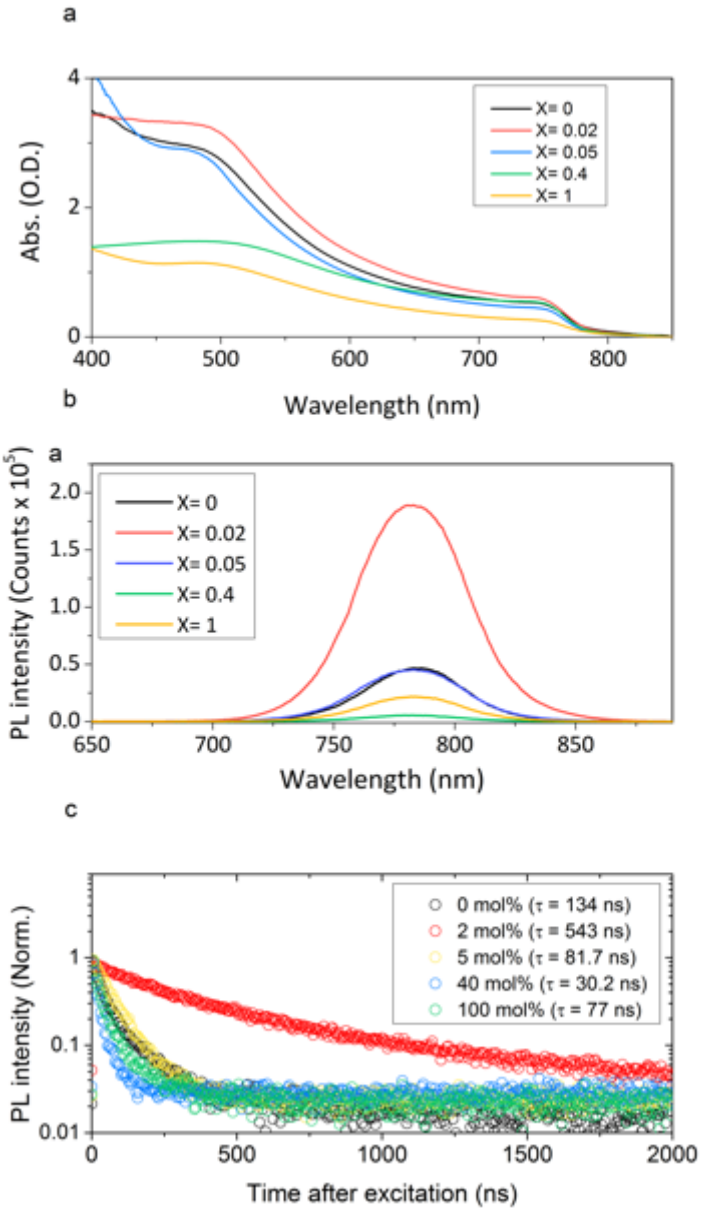

2 Figure S9. Photo-physical properties (a; UV-vis absorption, b; steady-state PL and c; time-
3 resolved PL) of the perovskite films fabricated from 3MAI:(1-x)$PbCl_2$:xPbI_2
4

Table S1. The corresponding PL quantum efficiency (PLQE) of the perovskite films fabricated from 3MAI:(1-x)$PbCl_2$:xPbI_2. For the time resolved PL the samples were excitedwith a 532 nm CW laser at 200 mW/cm^2.

X=	PLQE (%)
0	9.12±1.25
0.02	15.1±1.02
0.05	6.34±1.03
0.4	2.14± 0.37
1	1.96±1.29

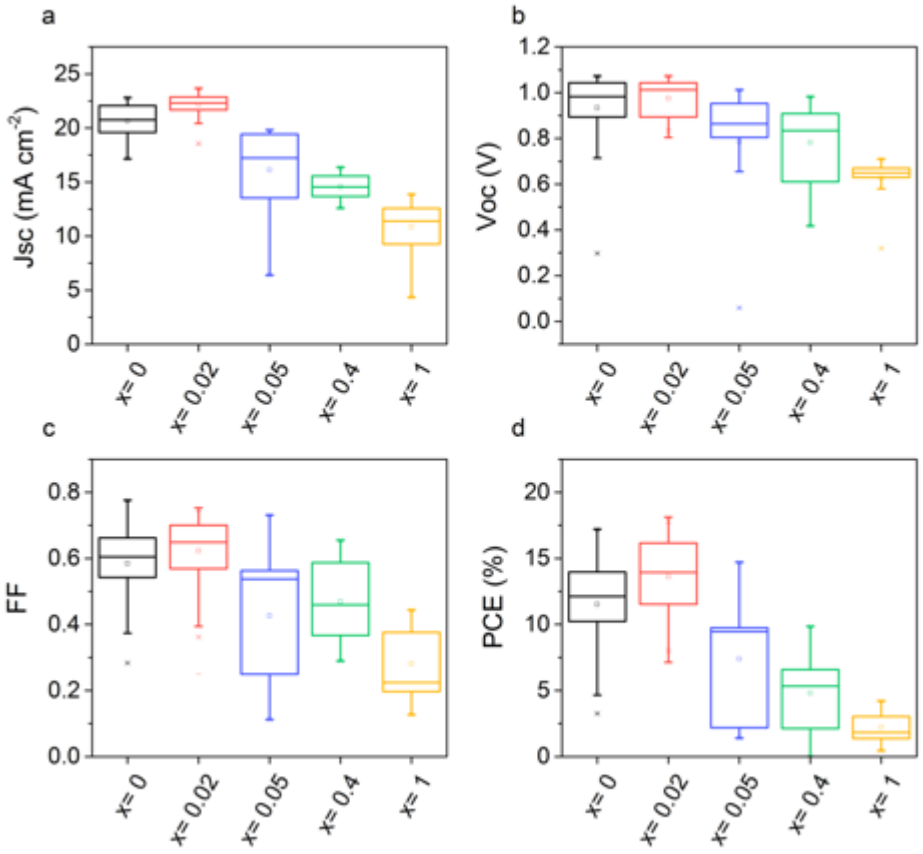

Figure S10. J-V performances of the perovskite solar cells fabricated from 3MAI:(1-x)$PbCl_2$:xPbI_2 precursor while varying PbI_2 content with x= 0, 0.02, 0.05, 0.4, 1. The device structure is FTO/TiO_2/Perovskite film/Spiro-OMeTAD/Ag.Each value from J-V sans are the average of data taken from 60 devices for the x= 0 and 0.02 and 10 devices for x=0.05, 0.4 and 1, respectively.

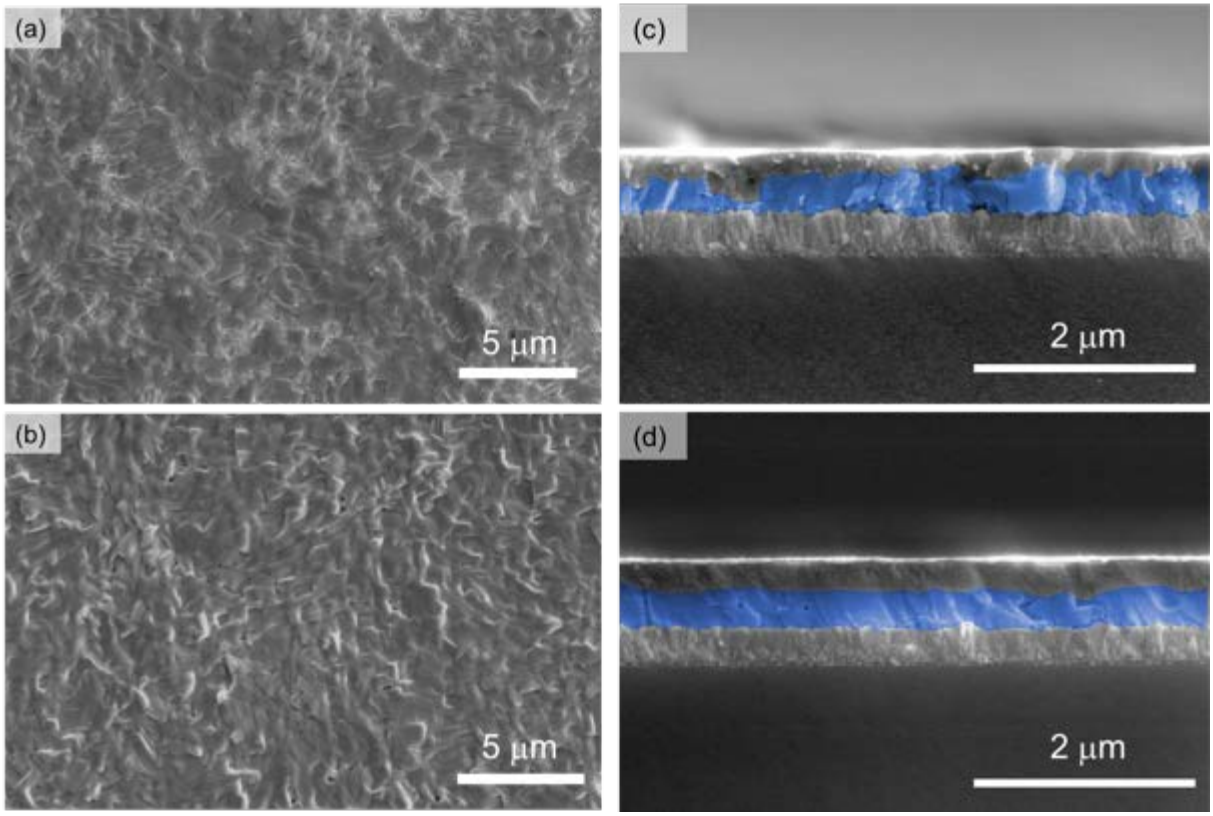

Figure S11. Top view SEM images of the perovskite film fabricated from (a) 3MAI:$PbCl_2$ (x = 0), and (b) 3MAI:0.98$PbCl_2$:0.02PbI_2(x = 0.02) starting solutions on TiO_2/C_{60} compact layer. Cross sectional SEM images of the complete perovskite solar cell of (a); x = 0 and (b); x = 0.02.

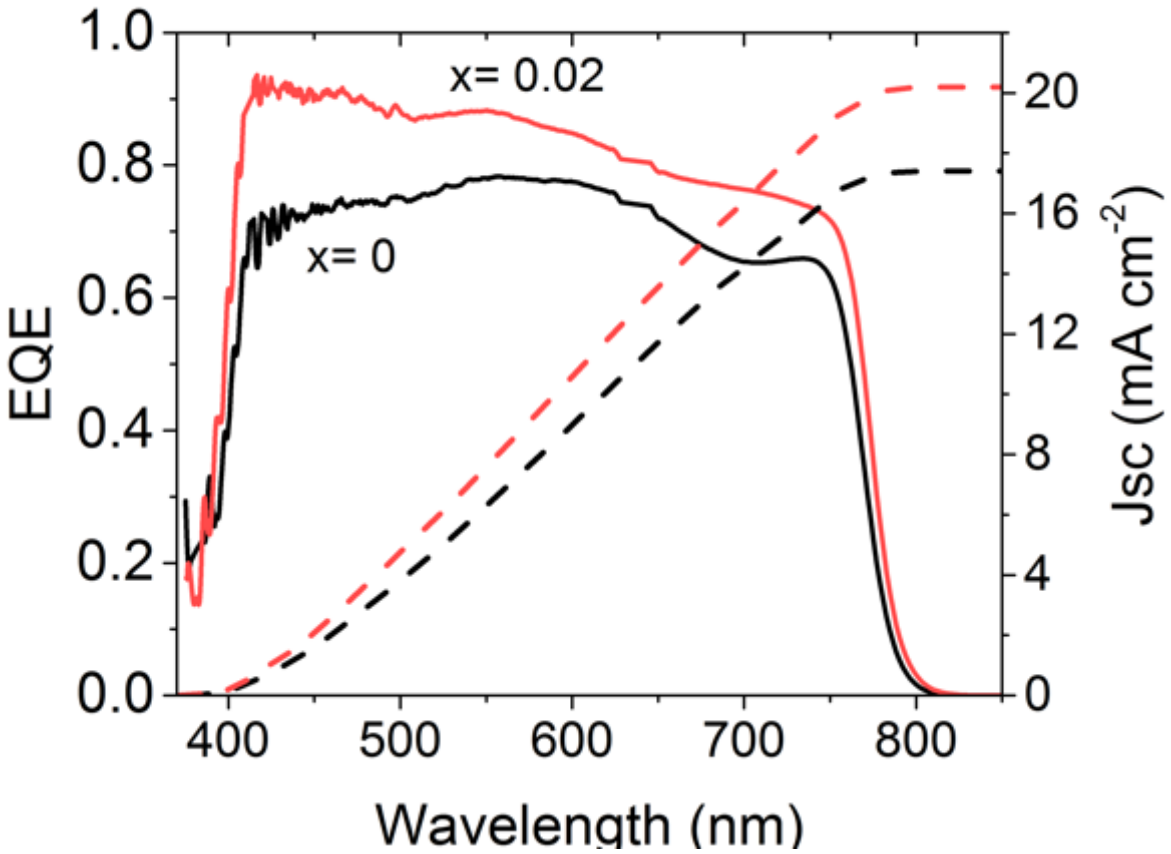

Figure S12. External quantum efficiency (EQE) spectra of the typical perovskite solar cells (FTO/TiO_2/C_{60}/$MAPbI_3$/Spiro-OMeTAD/Ag), fabricated from 3MAI:$PbCl_2$ (x = 0), and 3MAI:0.98$PbCl_2$:0.02PbI_2 (x = 0.02) starting solutions.

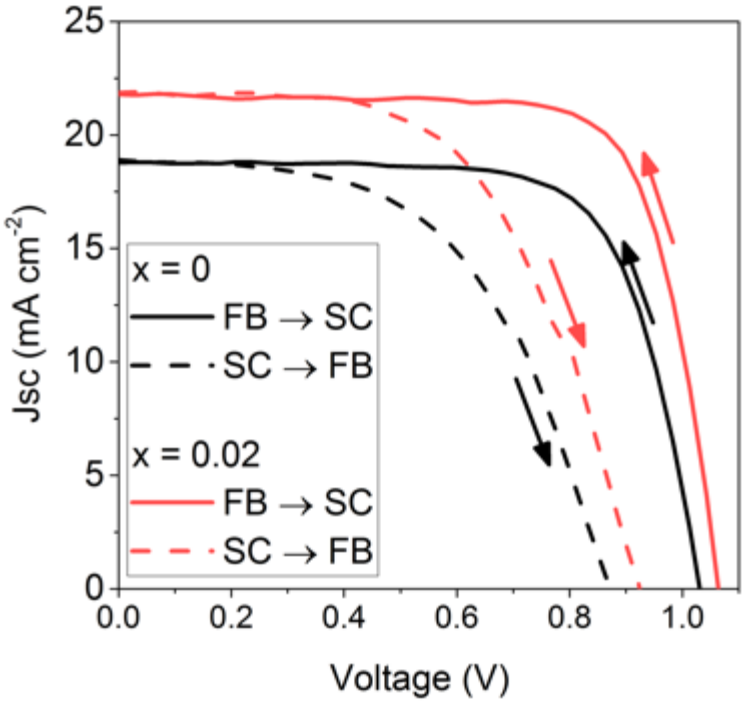

Figure S13. *JV* curves from both forward-bias to short-circuit (FB-SC) and short-circuit to forward-bias (SC-FB) current-voltage sweeps of the typical perovskite solar cells ($FTO/TiO_2/C_{60}/MAPbI_3$/Spiro-OMeTAD/Ag), fabricated from $3MAI:PbCl_2$ (x=0), and $3MAI:0.98PbCl_2:0.02PbI_2$ (x=0.02) starting solutions.

Reference

[1] I. Robinson, R. Harder, *Nat. Mater.* **2009**, *8*, 291.
[2] X.-L. W. A. Pramanick, X. P. Wang, C. Hoffmann, S. O. Diallo, M. R. V. Jørgensen, *Phys. Rev. B* **2015**, *92*, 174103.
[3] G. . Williamson, W. . Hall, *Acta Metall.* **1953**, *1*, 22.